RSC Advances

PAPER

View Article Online
View Journal | View Issue

Cite this: *RSC Adv.*, 2022, **12**, 13401

Magnetic coupling induced by the interaction between endohedral metal borofullerenes†

Jia Wang, * Xuhui Liu, Wanyi Zhang, Chunxu Wang and Zhengkun Qin*

Received 11th March 2022
Accepted 15th April 2022

DOI: 10.1039/d2ra01591a

rsc.li/rsc-advances

Superatom-assembled materials have highly tunable magnetic and electronic properties and parameters of clusters. Here, eight superatom dimers composed of two U@B_{40} motifs have been studied by the density functional theory. Calculation results show that U@B_{40} dimers exhibit spin antiferromagnetic coupling, spin ferromagnetic coupling and nonmagnetic, that is, the magnetic coupling is induced by the interaction between the U@B_{40} superatoms. In addition, the monomers in U@B_{40} dimers still retain the superatomic orbitals, and some of the super atomic orbitals disappear due to the interaction between monomers. The assembly based on U@B_{40} induced a decrease in the energy gap. This study provides a basis for a deep understanding of controlling the cluster-assembled materials for tailoring their functionalities.

Introduction

Cluster-assembled materials (CAMs) have attracted wide interest in recent years[1–4] and have been applied in organic pollutant sensing and biomedical applications,[5] gas sensors,[6,7] hydrogen storage,[8] *etc.* Thus, numerous CAMs have been studied, such as CdO and ZnO clusters,[9,10] TM@Si_{12} (TM = 3d transition metal),[11–13] $M_{12}N_{12}$ (M = Al, Ga) fullerene-like clusters[14] and noble metal nanostructures.[5,15–17] CAM building blocks are clusters, meaning, more atoms and arrangements are available to select and assemble to adjust the properties of the materials.[1] Stable cluster building blocks for self-assembly are of crucial importance, as many clusters at these small sizes have lifetimes too short for controlled assembly into materials.[1] In addition, clusters with closed electronic shells and large HOMO–LUMO (highest occupied molecular orbital-lowest unoccupied molecular orbital) gaps have enhanced stability and reduced reactivity.[18] Thus, superatoms, such as Al_{13}^-,[19–21] As_7,[22,23] B_{40},[24] C_{60},[25–27] An@C_{28},[28] can be used as building blocks in creating self-assembled cluster materials.

Previous studies on endohedral-metallofullerene (EMF) containing actinides have promoted the application of actinide compounds in functional nanomaterials and nanomedicine.[29–31] In 2014, a combination of experimental and theoretical research discovered the B_{40} hollow cage.[32] Subsequently, studies have shown that B_{40} clusters exhibit superatomic properties, but their electronic configuration is not fully filled.[33] Moreover, the clusters of embedded atoms or small molecules can form stable core@shell systems.[34,35] The studies on U@B_{40} prove that it is indeed a stable closed-shell electronic structure.[35] Therefore, the U@B_{40} as building blocks for assembly are capable of tailoring more stable nanostructures or nanocrystals. Moreover, the interaction between EMFs of U@C_{28} can lead to different chemical and physical adsorption structures, which are derived from different magnetic coupling.[36] Whether the interaction between U@B_{40} superatoms also causes magnetic coupling, will be helpful for the study of functional CAMs.

Currently, cluster-assembled materials are explored and tailored to control their functions.[1] In this work, we constructed eight U@B_{40} dimers based on the first principles. Unlike the U@B_{40} monomer,[35] the assembly based on U@B_{40} affects the magnetic properties of the structures, and different conformations exhibit different magnetic coupling. The monomers in the U@B_{40} dimer also retain part of the superatomic orbitals, similar to the assembly of B_{40} oligomers.[24] The energy gap of the U@B_{40} dimer is smaller than that of U@B_{40}.[35] Therefore, we propose a possible route to construct cluster-assembled materials using U@B_{40} superatoms.

Models and computational methods

The U@B_{40} has two hexagons (6_1 and 6_2) and four heptagons (7_1–7_4), as the lower right corner of Fig. 1. In this work, we enumerated various possible directions along the two U@B_{40} and obtained eight U@B_{40} dimers, and arranged them according to their total energies. Structure (a) is formed by the 7_3 heptagons of one U@B_{40} stacked onto the vertical 7_1 heptagons of another (denoted as $7_3 \perp 7_1$); it has the lowest total energy. Structures (b) and (c) are formed by 7_3 heptagons of one cluster parallel and antiparallel to 7_1 heptagons of another (denoted as

College of Information Technology, Jilin Normal University, Siping 136000, China. E-mail: wangjia18@jlnu.edu.cn; qzkjlnu@163.com

† Electronic supplementary information (ESI) available: The relative energies, molecular orbitals diagram and density of states. See https://doi.org/10.1039/d2ra01591a

$7_3\nearrow\nearrow 7_1$ and $7_3\nearrow\swarrow 7_1$, respectively). Structures (d), (e), (g) and (h) are formed by the 7_3 heptagons or 6_1 hexagons of one cluster stacked onto the 6_1 or 6_2 hexagons of another. The structure (f) is formed by the B atoms of one cluster connecting to the B atoms of another cluster (represented as vertex–vertex). The relative energies between other structures and the lowest energy structure ($7_3\perp 7_1$) are placed in brackets in Fig. 1. The relative energies of the U@B_{40} dimers are listed in Table S1† in the ESI. Since the energy of the conformation $7_3\perp 7_1$ is the lowest, the following analysis and discussion are mainly performed on it.

The Amsterdam density functional package (ADF, 2012.01)[38] was employed to perform calculations. To ensure the reliability of the obtained structures, geometry optimizations were performed without imposing any symmetry constraints. All calculations presented in this work were performed using Perdew–Burke–Ernzerhof (PBE)[39] generalized gradient approximation exchange–correlation functionals. Scalar relativistic effects were accounted for using the zero-order regular approximation (ZORA) method. TZ2P Slater basis sets (relativistic valence triple-ζ) with two polarization functions were employed,[40] and the frozen-core approximation was used for 1s–4f electrons of the uranium atom. The empirical dispersion-corrected density functional theory (DFT-D3)[41] was used to fully obtain the intermolecular interaction of the U@B_{40} structures.

Results and discussion

The spin polarization of U@B_{40} dimers was analyzed and the results were different from those of U@B_{40} without spin polarization.[35] As shown in Fig. 2, the spin orientation of one U@B_{40} monomer in the $7_3\perp 7_1$, $7_3\nearrow\nearrow 7_1$ and 6_1–6_2 conformations is spin-up, and that of another monomer is spin-down. The spin orientations of the two monomers are opposite, thus exhibiting the spin antiferromagnetic coupling phenomenon, which is consistent with $(U@C_{28})_2$.[42] For $7_3\nearrow\swarrow 7_1$, vertex–vertex and 7_3–6_2 conformations, the spin orientations of the two U@B_{40} monomers are spin-up, and thus exhibiting spin ferromagnetic coupling. Distinct from 7_3–6_2, although the ground state of 7_3–6_1 conformation is also a triplet state, the two unpaired electrons are occupied on one monomer. Thus, one U@B_{40} monomer exhibits spin polarization, while another monomer has no spin polarization (shown in Fig. 2(d)). In addition, the ground state of the 6_1–6_1 structure is a closed-shell singlet state without spin polarization, similar to U@B_{40}.[35] The results show that different U@B_{40} dimers exhibit different spin polarization phenomena, thus U@B_{40} as the motif for assembly can affect the magnetic properties.

To further explore the origin of the spin-polarized phenomenon, the MOs of U@B_{40} dimers were analyzed. There are 232 α and 232 β MOs of the conformation $7_3\perp 7_1$, and the frontier MOs diagram is shown in Fig. 3. The HOMO for the α electron (denoted as HOMOα) is strongly localized on one U@B_{40}

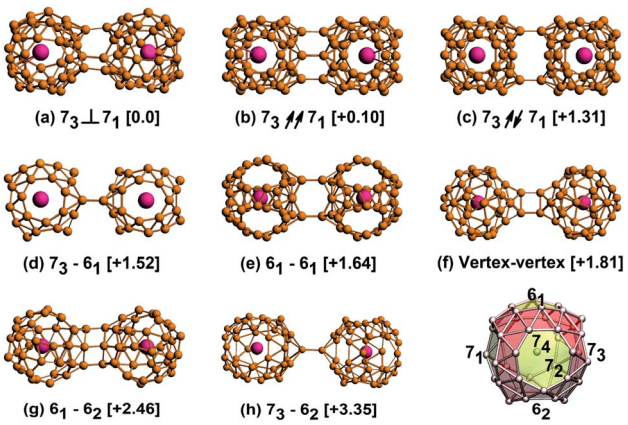

Fig. 1 Structure diagrams for all the isomers formed by the interaction between two U@B_{40} superatoms. (a) Stacking the 7_3 heptagons of one cluster vertical to the 7_1 heptagons of another. (b and c) Stacking the 7_3 heptagons of one cluster parallel or antiparallel to the 7_1 heptagons of another. (d and e) Stacking the 7_3 heptagons or 6_1 hexagons of one cluster onto the 6_1 hexagons of another. (f) Connecting the B atoms of one cluster with the B atoms of another cluster. (g and h) Stacking the 6_1 hexagons or 7_3 heptagons of one cluster onto the 6_2 hexagons of another. The values in brackets are the relative energies between each isomer and the lowest energy structure, given in eV. The structure of the U@B_{40} is shown in the lower right corner. A similar drawing method refers to ref. 24 and 37.

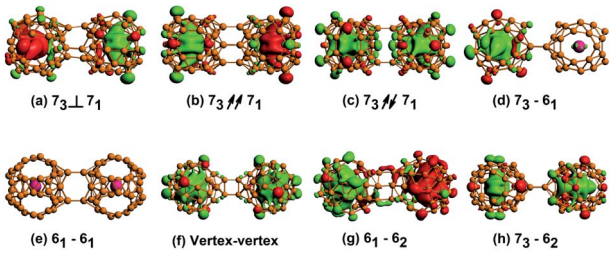

Fig. 2 Spin density diagram of U@B_{40} dimers for eight conformations. The green region represents spin up and the red region represents spin down. The isosurface value is 0.01 a.u.

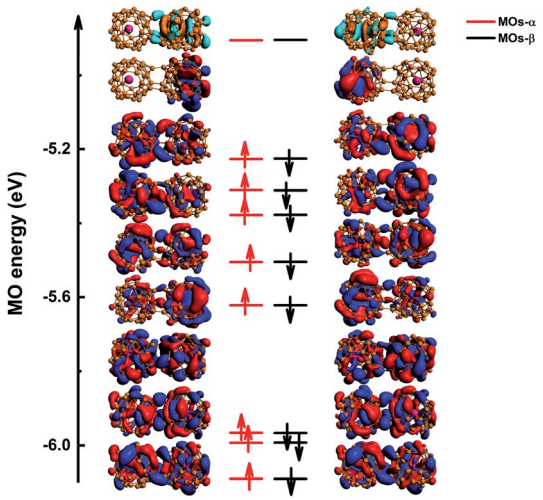

Fig. 3 The frontier molecular orbital (MOs) diagram of the ground state of $7_3\perp 7_1$ conformations. The red and black lines represent α-MOs and β-MOs, respectively. The MOs indicated by blue and red are occupied MOs, while those indicated by orange and cyan are unoccupied MOs. The isosurface value is 0.01 a.u.

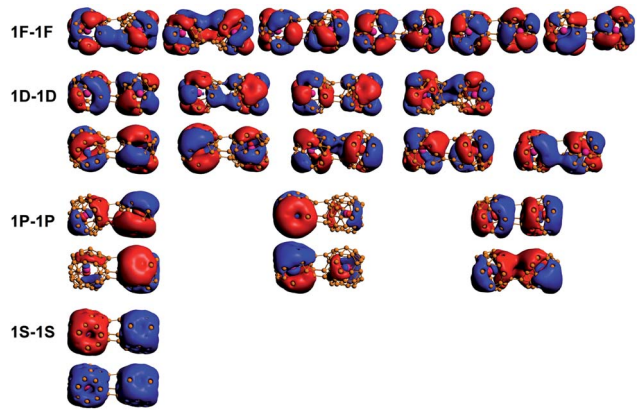

Fig. 4 The MOs diagram for α electrons of $7_3 \perp 7_1$ confirmations for the U@B_{40} superatomic orbital components. Superatomic orbitals 1S, 1P, 1D, and 1F are composed of the B_{40} cages. The blue and red areas indicate the positive and negative signs of the wave functions, respectively. Isovalue = 0.02 a.u.

Fig. 5 MOs-α of the $7_3 \perp 7_1$ conformations for the U@B_{40} superatomic orbital components. 2S, 2P, 2D, and 2F refer to the U@B_{40} monomer superatomic orbitals.

monomer, while the HOMO for β electron (HOMOβ) mainly occupies another monomer. The other occupied MOs were delocalized on the U@B_{40} dimer. Therefore, the spin density of $7_3 \perp 7_1$ conformations is mainly contributed by HOMOα and HOMOβ. The spin density for spin-up comes from HOMOα, while that for spin-down derives from HOMOβ, thus exhibiting spin antiferromagnetic coupling. Furthermore, the MOs of other U@B_{40} dimers were also analyzed, and the results show that the spin density comes from the frontier MOs of structures (as shown in Fig. S1–S7†).

Previous studies on B_{40} oligomers have shown that B_{40} monomers still retain superatomic properties.[24] Similarly, the superatomic MOs of $7_3 \perp 7_1$ conformations were also analyzed in detail. In the MOs with lower energy levels, we found that the monomeric superatomic orbitals are composed of B_{40} cages. While superatomic orbitals are contributed by the 2s orbital of B atoms, similar to the superatomic orbital 1S, 1P, 1D and 1F of B_{40} (ref. 33) (as shown in Fig. 4). The superatomic MOs of two monomers cooperate in in-phase and out-of-phase cooperation, denoted as 1S–1S, 1P–1P, 1D–1D, 1F–1F. In the MOs with higher energy levels, the U@B_{40} monomer still retains superatomic MOs, and the superatomic orbitals are a hybridization of the 7s, 7p, 6d, and 5f orbitals of the U atom with the B_{40} cage orbitals.[35] The superatomic MOs of two U@B_{40} monomers cooperate in in-phase and out-of-phase, denoted as 2S–2S, 2P–2P, 2D–2D, 2F–2F, as shown in Fig. 5. However, U@B_{40} exhibits a 32-electron closed-shell singlet configuration.[35] There should be two S–S, six P–P, ten D–D and fourteen F–F superatomic MOs in accordance with the in-phase and out-of-phase cooperation between each other. Here, we found that some monomeric superatomic orbitals disappeared due to the stronger orbital interaction. The disappearance of 1D–1D MOs is caused by the distortion of the B_{40} cages and the disappearance of 2D–2D and 2F–2F MOs result from the deviation of the U atom from the cage center. Fig. 4 and 5 are the superatomic MOs diagrams of α electrons, and the superatomic MOs diagrams of β electrons are shown in Fig. S8 and S9† in ESI. In addition, we also analyzed the MOs of

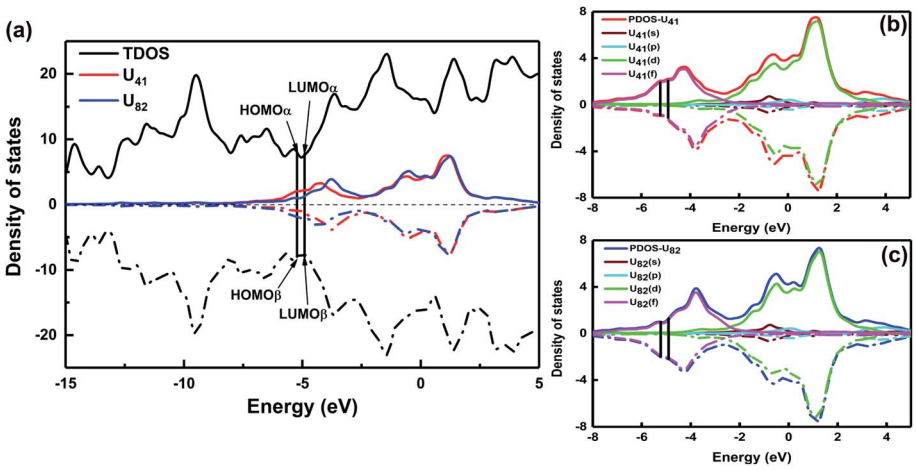

Fig. 6 Density of states of structure $7_3 \perp 7_1$. (a) The total density of states (TDOS) of $7_3 \perp 7_1$ and the local density of states (LDOS) of U atoms. (b) and (c) The partial density of states (PDOS) of s, p, d, and f atomic orbital of two U atoms.

Table 1 The HOMO–LUMO gap of U@B_{40} dimers

The HOMO–LUMO gap (eV)							
$7_3 \perp 7_1$	$7_3 \nearrow \nearrow 7_1$	$7_3 \nearrow \swarrow 7_1$	7_3–6_1	6_1–6_1	Vertex–vertex	6_1–6_2	7_3–6_2
0.32	0.32	0.27	0.16	0.45	0.30	0.30	0.12

6_1–6_1 conformation, as this conformation is less twisted and the U atom is not severely deviated from the B_{40} cage center. The results show that only two 2F–2F MOs disappeared, as shown in Fig. S10† in the ESI.

To further explore the orbital composition, the density of states of $7_3 \perp 7_1$ conformations was analyzed. The total density of states (TDOS) of the U@B_{40} dimer for $7_3 \perp 7_1$ conformations, the local density of states (LDOS) and the partial density of states (PDOS) of U atoms are displayed in Fig. 6. The results demonstrate that U atoms in $7_3 \perp 7_1$ conformations mainly contribute to frontier and unoccupied MOs, and the occupied MOs are mainly contributed by the 5f orbitals of the U atoms. Therefore, 1S–1S, 1P–1P, 1D–1D and 1F–1F MOs are composed of B_{40} cages, and 2S–2S, 2P–2P, 2D–2D, 2F–2F MOs are composed of B_{40} cages and U atoms. Further, the DOS of other U@B_{40} dimers, $7_3 \nearrow \swarrow 7_1$, 7_3–6_1, 6_1–6_1 and 6_1–6_2, were also analyzed (as shown in Fig. S11–S14†). Furthermore, the HOMO–LUMO gap of the U@B_{40} dimers was analyzed, as listed in Table 1. The results showed that the HOMO–LUMO gap of the eight conformations of U@B_{40} dimers are 0.32 eV, 0.32 eV, 0.27 eV, 0.16, 0.45 eV, 0.30 eV, 0.30 eV and 0.12 eV, respectively. While the HOMO–LUMO gap of U@B_{40} was 0.76 eV.[35] Therefore, U@B_{40} assembly causes a reduction in the energy gap, which is similar to the result of previous studies on B_{40} superatom-assembly.[24]

Conclusions

In this study, U@B_{40} superatom dimers were investigated using the first principles. The results show that different U@B_{40} dimers exhibit different spin polarization phenomena, they have spin antiferromagnetic coupling, spin ferromagnetic coupling and nonmagnetic. As such, the magnetic coupling can be tuned according to different types of the U@B_{40} assembly. Moreover, the spin density mainly comes from the frontier MOs. Further analysis of the MOs revealed that the monomer of the U@B_{40} dimers still retained some superatomic properties. One kind of superatomic orbital is composed of B_{40} cages and another kind of superatomic orbital is composed of B_{40} and U atoms. In addition, the U@B_{40} superatomic assembly causes the energy gap to decrease. This work mainly studied the interaction between embedded metal fullerenes, which provides a new idea for cluster assembly materials.

Author contributions

Jia Wang calculated and analyzed the results. All the authors contributed to the general discussion.

Conflicts of interest

There are no conflicts to declare.

Acknowledgements

This work was financially supported by the National Natural Science Foundation of China (grant number 11947039), the Natural Science Foundation Project of Jilin Province (grant number YDZJ202101ZYTS075).

Notes and references

1 S. A. Claridge, A. W. Castleman Jr, S. N. Khanna, C. B. Murray, A. Sen and P. S. Weiss, *ACS Nano*, 2009, **3**, 244–255.
2 S. Mandal, A. C. Reber, M. Qian, P. S. Weiss, S. N. Khanna and A. Sen, *Acc. Chem. Res.*, 2013, **46**, 2385–2395.
3 J. Schmelzer Jr, S. A. Brown, A. Wurl, M. Hyslop and R. J. Blaikie, *Phys. Rev. Lett.*, 2002, **88**, 226802.
4 Q. D. Liu and X. Wang, *InfoMat*, 2021, **3**, 854–868.
5 A. Nag, P. Chakraborty, A. Thacharon, G. Paramasivam, B. Mondal, M. Bodiuzzaman and T. Pradeep, *J. Phys. Chem. C*, 2020, **124**, 22298–22303.
6 Y. Yong, X. Su, Q. Zhou, Y. Kuang and X. Li, *Sci. Rep.*, 2017, **7**, 17505.
7 Y. Yong, H. Jiang, X. Li, S. Lv and J. Cao, *Phys. Chem. Chem. Phys.*, 2016, **18**, 21431–21441.
8 C. S. Liu, H. An, L. J. Guo, Z. Zeng and X. Ju, *J. Chem. Phys.*, 2011, **134**, 024522.
9 R. Łazarski, M. Sierka, J. Heinzelmann, A. Koop, R. Sedlak, S. Proch and G. F. Ganteför, *J. Phys. Chem. C*, 2015, **119**, 6886–6895.
10 Y. L. Yong, B. Song and P. M. He, *J. Phys. Chem. C*, 2011, **115**, 6455–6461.
11 Z. Liu, X. Wang, J. Cai and H. Zhu, *J. Phys. Chem. C*, 2015, **119**, 1517–1523.
12 Z. Nie, P. Guo, J. Zheng, P. Zhao, Y. Wan and Z. Jiang, *Comput. Mater. Sci.*, 2018, **146**, 134–142.
13 K. Dhaka and D. Bandyopadhyay, *Dalton Trans.*, 2016, **45**, 12432–12443.
14 Y. Yong, B. Song and P. He, *Phys. Chem. Chem. Phys.*, 2011, **13**, 16182–16189.
15 Y. Song, F. Fu, J. Zhang, J. Chai, X. Kang, P. Li, S. Li, H. Zhou and M. Zhu, *Angew. Chem., Int. Ed.*, 2015, **54**, 8430–8434.
16 J. Y. Wang, R. W. Huang, Z. Wei, X. J. Xi, X. Y. Dong and S. Q. Zang, *Chem.–Eur. J.*, 2019, **25**, 3376–3381.
17 M. Cao, R. Pang, Q. Y. Wang, Z. Han, Z. Y. Wang, X. Y. Dong, S. F. Li, S. Q. Zang and T. C. W. Mak, *J. Am. Chem. Soc.*, 2019, **141**, 14505–14509.
18 A. C. Reber and S. N. Khanna, *Acc. Chem. Res.*, 2017, **50**, 255–263.
19 A. C. Reber, S. N. Khanna and A. W. Castleman Jr, *J. Am. Chem. Soc.*, 2007, **129**, 10189–10194.
20 W. J. Zheng, O. C. Thomas, T. P. Lippa, S. J. Xu and K. H. Bowen Jr, *J. Chem. Phys.*, 2006, **124**, 144304.

21 F. Liu, M. Mostoller, T. Kaplan, S. N. Khanna and P. Jena, *Chem. Phys. Lett.*, 1996, **248**, 213–217.
22 A. W. Castleman and S. N. Khanna, *J. Phys. Chem. C*, 2009, **113**, 2664–2675.
23 A. W. Castleman Jr, S. N. Khanna, A. Sen, A. C. Reber, M. Qian, K. M. Davis, S. J. Peppernick, A. Ugrinov and M. D. Merritt, *Nano Lett.*, 2007, **7**, 2734–2741.
24 J. Wang, W. R. Jiang, W. Y. Xie, J. P. Wang and Z. G. Wang, *Sci. China Mater.*, 2019, **62**, 416–422.
25 C. A. Mirkin and W. B. Caldwell, *Tetrahedron*, 1996, **52**, 5113–5130.
26 F. Diederich and C. Thilgen, *Science*, 1996, **271**, 317–323.
27 X. Roy, C. H. Lee, A. C. Crowther, C. L. Schenck, T. Besara, R. A. Lalancette, T. Siegrist, P. W. Stephens, L. E. Brus and P. Kim, *Science*, 2013, **341**, 157.
28 P. Pyykkö, C. Clavaguéra and J.-P. Dognon, *Comput. Methods Lanthanide Actinide Chem.*, 2015, 401–424.
29 T. Guo, M. D. Diener, Y. Chai, M. J. Alford, R. E. Haufler, S. M. McClure, T. Ohno, J. H. Weaver, G. E. Scuseria and R. E. Smalley, *Science*, 1992, **257**, 1661–1664.
30 P. W. Dunk, N. K. Kaiser, M. Mulet-Gas, A. Rodríguez-Fortea, J. M. Poblet, H. Shinohara, C. L. Hendrickson, A. G. Marshall and H. W. Kroto, *J. Am. Chem. Soc.*, 2012, **134**, 9380–9389.
31 D. Wang, W. F. van Gunsteren and Z. Chai, *Chem. Soc. Rev.*, 2012, **41**, 5836–5865.
32 H.-J. Zhai, Y.-F. Zhao, W.-L. Li, Q. Chen, H. Bai, H.-S. Hu, Z. A. Piazza, W.-J. Tian, H.-G. Lu, Y.-B. Wu, Y.-W. Mu, G.-F. Wei, Z.-P. Liu, J. Li, S.-D. Li and L.-S. Wang, *Nat. Chem.*, 2014, **6**, 727–731.
33 J. Wang, T. Yu, Y. Gao and Z. Wang, *Sci. China Mater.*, 2017, **60**, 1264–1268.
34 X. Dai, Y. Gao, W. Jiang, Y. Lei and Z. Wang, *Phys. Chem. Chem. Phys.*, 2015, **17**, 23308–23311.
35 T. Yu, Y. Gao, D. Xu and Z. Wang, *Nano Res.*, 2018, **11**, 354–359.
36 W. Xie, W. Jiang, Y. Gao, J. Wang and Z. Wang, *Chem. Commun.*, 2018, **54**, 13383–13386.
37 Y. Yang, Z. Zhang, E. S. Penev and B. I. Yakobson, *Nanoscale*, 2017, **9**, 1805–1810.
38 G. te Velde, F. M. Bickelhaupt, E. J. Baerends, C. Fonseca Guerra, S. J. A. van Gisbergen, J. G. Snijders and T. Ziegler, *J. Comput. Chem.*, 2001, **22**, 931–967.
39 J. P. Perdew, K. Burke and M. Ernzerhof, *Phys. Rev. Lett.*, 1996, **77**, 3865–3868.
40 E. Van Lenthe and E. J. Baerends, *J. Comput. Chem.*, 2003, **24**, 1142–1156.
41 S. Grimme, J. Antony, S. Ehrlich and H. Krieg, *J. Chem. Phys.*, 2010, **132**, 154104.
42 W. Y. Xie, Y. Zhu, J. P. Wang, A. H. Cheng and Z. G. Wang, *Chin. Phys. Lett.*, 2019, **36**, 116401.